Journal of Power Electronics (2022) 22:1100–1111
https://doi.org/10.1007/s43236-022-00419-9

ORIGINAL ARTICLE

Adaptive active damping method of grid-connected inverter based on model predictive control in weak grid

Ruinan Xue[1] · Guojin Li[1] · Hengzhou Tong[1] · Yanming Chen[1]

Received: 19 October 2021 / Revised: 9 March 2022 / Accepted: 14 March 2022 / Published online: 4 April 2022

Abstract

The LCL-type grid-connected inverter based on finite control set model predictive control (FCS-MPC) is suitable for weak grids because of its good robustness and fast dynamic response. However, in an FCS-MPC-based system, the variable switching frequency causes the spread of the inverter-side current harmonic spectrum. Thus, the grid-side current may be distorted because the harmonics are amplified to the grid side due to the resonance peak of the LCL filter. To solve the above problem, this paper proposes an adaptive active damping (AD) method to eliminate the resonant effects. First, the system based on an MPC controller is regarded as a closed-loop system of the grid-side current, and the resonance peak is suppressed effectively by an AD, which consists of a virtual resistor and a virtual capacitor. Second, to balance the resonance suppression and dynamic performance of the system under weak grid conditions, the grid impedance is measured and the optimal AD values for different grid impedance are calculated online. Compared with the fixed-value AD, the proposed method has better resonance suppression and higher bandwidth. The effectiveness and feasibility of the proposed control strategy are verified by simulations and experiments.

Keywords LCL-type grid-connected inverter · Weak grid · Finite control set model predictive control · Impedance identification · Adaptive active damping method

1 Introduction

LCL-type grid-connected inverters are widely employed in renewable energy systems because of their good switching ripple attenuation and small sizes. However, under weak grid conditions, the varied grid impedance challenges the stability of the conventional LCL filter-based current controlled system [1]. Therefore, to improve the adaptability of the grid-connected inverters to weak grids, modern control strategies that provide good robustness such as sliding mode control [2], neural network algorithm [3], or predictive control schemes [4–6] can be alternatives to the conventional control approaches.

Recently, finite control set model predictive control (FCS-MPC) has been widely used in inverters with LC filter [7] and L filter [8–11], while inverters with LCL filter have more advantages in increasing the mitigation of switching harmonics with smaller components [12–15]. The FCS-MPC strategies, which are applied to the LCL-type grid-connected inverter, can be classified into inverter-side current control, grid-side current control, and multivariable control. In these control methods, the inverter-side current control has the least sensitivity to parameter variations [14]; thus, it is more suitable for weak grid conditions. Even so, the grid-side current may be distorted due to the spread of the inverter-side current harmonic spectrum and the harmonic amplification of the LCL-filter resonance peak. Therefore, an additional active damping (AD) is necessary.

In conventional linear control strategies, capacitor–current feedback AD method [16–18], capacitor–voltage feedback AD method [19, 20], and multiple state variables feedback AD method [21] are extensively used in PWM-based systems to eliminate the resonant effects. Generally, the principle of the above methods can be regarded as the different state variables added to the PWM modulation wave. FCS-MPC is nonlinear and does not have a modulator; thus, the conventional AD method cannot be directly applied to the FCS-MPC-based inverter. Nowadays, frequency-weighted predictive control [22, 23] and the virtual resistance (VR)

✉ Yanming Chen
yanmingchen@gxu.edu.cn

1 School of Electrical Engineering, Guangxi University, Nanning, China

AD method [24, 25] are proposed to eliminate the resonant effects in FCS-MPC-based systems. In frequency-weighted predictive control strategies, a notch filter is added to the cost function to shape the current harmonic spectrum [22]. On this basis, an adaptive notch filter is designed based on the least mean square (LMS) algorithm [23]. However, the LMS algorithm requires multiple iterations to train the appropriate notch filter coefficients, thus reducing the practicability of this method. In VR AD strategies, to attenuate the grid current harmonics, the capacitor voltage is filtered by a digital high-pass filter, and the filtered signal is added to the inverter-side current reference by the virtual resistance [24, 25]. However, these methods are studied under strong grid conditions and without the consideration of the influence of the grid impedance on the system. The optimal selection of AD parameters has not been analyzed either.

In this paper, an adaptive AD method for the grid-connected inverter based on FCS-MPC is proposed. The AD, which consists of a virtual resistor in series with a virtual capacitor (virtual RC), is applied to reduce the grid current harmonics caused by the resonance peak. Moreover, the influence of the varied grid impedance on the AD resonance suppression is analyzed, and an adaptive AD algorithm based on grid impedance identification is studied. The effectiveness of the proposed control strategy is validated by simulations and experiments.

The remainder of this paper is organized as follows. In Sect. 2, a discrete-time model of the LCL-type grid-connected inverter is established, and a current controller based on FCS-MPC is designed. In Sect. 3, an AD method with virtual RC is proposed. In Sect. 4, an adaptive AD algorithm is designed for weak grid conditions. In Sect. 5, an analysis of simulation and experimental results is presented. Finally, in Sect. 6, the conclusion is given.

2 FCS-MPC strategy of the LCL-type grid-connected inverter

The main circuit of the single-phase LCL-type grid-connected inverter under a weak grid condition is shown in Fig. 1. The LCL filter is composed of the inverter-side inductance L_1, the filter capacitor C, and the grid-side inductance L_2. U_{dc} is the DC-link voltage. u_{pcc}, u_g, and L_g are the point of common coupling (PCC) voltage, grid voltage, and grid impedance, respectively.

To build a model for predictive control, the LCL-type grid-connected inverter circuit is simplified and the equivalent circuit is shown in Fig. 2, where u_{inv} is the output voltage of the inverter. u_c is the capacitor voltage. i_1 and i_2 are the inverter-side current and the gird-side current, respectively.

The differential equations of the circuit are given by

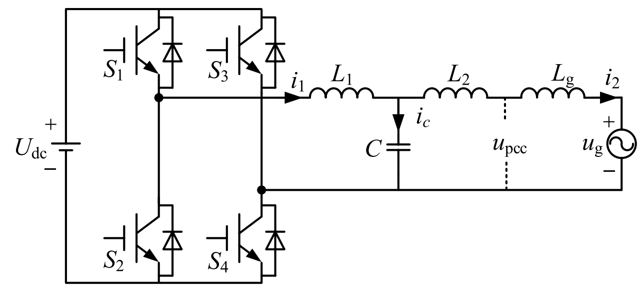

Fig. 1 Main circuit of single-phase LCL-type grid-connected inverter in a weak grid condition

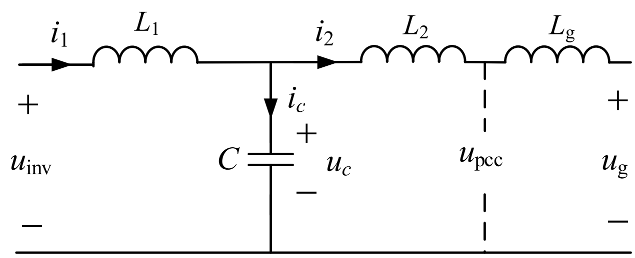

Fig. 2 Equivalent circuit of LCL-type grid-connected inverter under a weak grid condition

$$\begin{cases} C\dfrac{\mathrm{d}u_c}{\mathrm{d}t} = i_1 - i_2 \\ (L_2 + L_g)\dfrac{\mathrm{d}i_2}{\mathrm{d}t} = u_c - u_g \\ L_1\dfrac{\mathrm{d}i_1}{\mathrm{d}t} + u_c = u_{inv} \end{cases}. \tag{1}$$

The backward difference scheme is used to discretize the first and second equations of (1) with a sampling time T_s. The reference value of the inverter-side current at time k is given by (2), where i_{2ref} is the reference value of the grid-side current i_2, and its phase is synchronized with u_{pcc}:

$$\begin{cases} i_{1ref}(k) = i_{2ref}(k) + C\dfrac{u_{cref}(k) - u_{cref}(k-1)}{T_s} \\ u_{cref}(k) = (L_2 + L_g)\dfrac{i_{2ref}(k) - i_{2ref}(k-1)}{T_s} + u_g(k) \end{cases}. \tag{2}$$

Through the discretization of the third equation of (1) using the forward difference scheme, the future inverter-side current $i_1(k+1)$ is given by

$$i_1(k+1) = \frac{T_s}{L_1}\left(u_{inv}(k) - u_c(k)\right) + i_1(k), \tag{3}$$

where $u_{inv}(k)$ is determined by the state of the four switches S_1–S_4. If $S_n = 1$, then the switch is turned on; if $S_n = 0$, then

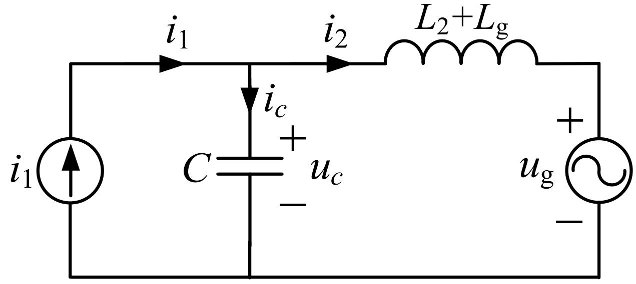

Fig. 3 Equivalent output stage of the system without damping

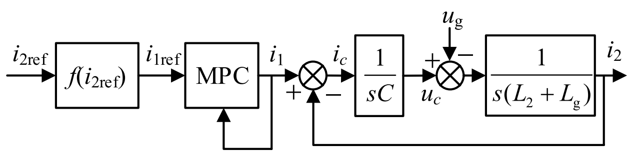

Fig. 4 Control block diagram of the system without damping

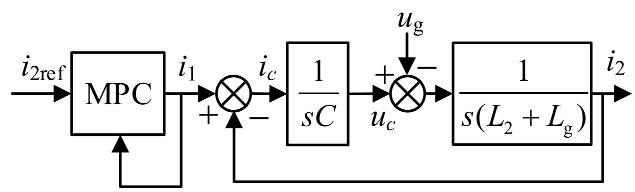

Fig. 5 Simplified control block diagram of the system

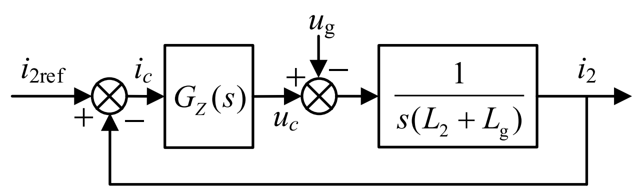

Fig. 6 Closed-loop control system of the grid-side current

the switch is turned off. Considering the different states of S_1–S_4, (1, 0, 0, 1), (0, 1, 1, 0), (1, 0, 1, 0), (0, 1, 0, 1) are obtained. If (S_1, S_2, S_3, S_4) = (1, 0, 0, 1), then $u_{inv} = U_{dc}$; if (S_1, S_2, S_3, S_4) = (0, 1, 1, 0), then $u_{inv} = -U_{dc}$; if (S_1, S_2, S_3, S_4) = (1, 0, 1, 0) or (0, 1, 1, 0), then $u_{inv} = 0$. (1, 0, 1, 0) is used as the switching state for $u_{inv} = 0$. Therefore, three available switching states exist in this MPC strategy.

When T_s is sufficiently small, $i_{1ref}(k+1) \approx i_{1ref}(k)$ can be assumed; thus, the cost function g_j is defined by

$$g_j = \left(i_{1ref}(k) - i_1(k+1)\right)^2, \tag{4}$$

where $j = 1, 2, 3$, and the switching state that corresponds to the minimum value of g_j is applied to the next sampling period.

3 Method of virtual RC damping

Considering that FCS-MPC is a nonlinear control strategy, designing an AD using the analysis method of linear systems is difficult. This paper simplifies the MPC-based system at first; thus, the system based on an FCS-MPC controller can be regarded as a closed-loop system of the grid-side current.

3.1 Simplification of the MPC-based system

As the direct control object of the system is the inverter-side current i_1 and the response speed of the MPC controller is relatively fast, u_{inv} and L_1 can be considered as a current source i_1 [26]. The simplified circuit is shown in Fig. 3, and the control block diagram of the system is shown in Fig. 4.

From Fig. 3, the relationship between $|i_{2ref}|$ and $|i_{1ref}|$ is given by

$$\left|i_{2ref}\right| = \left|i_{1ref}\right| \frac{|Z_c|}{|Z_c| + |Z_2|} - \frac{\left|u_g\right|}{|Z_c| + |Z_2|}, \tag{5}$$

where $|i_{1ref}|$, $|i_{2ref}|$ and $|u_g|$ are the amplitude of i_{1ref}, i_{2ref}, and u_g, respectively. $|Z_c|$ and $|Z_2|$ are the impedance modulus of the filter capacitor C and $L_2 + L_g$.

At the fundamental frequency (50 Hz), when $C = 4.7$ μF, $|Z_c| \approx 680$ Ω; when $L_2 + L_g = 0.6$–8.6 mH, $|Z_2| = 0.2$ Ω–2.6 Ω. Therefore, (5) can be simplified to

$$\left|i_{2ref}\right| = \left|i_{1ref}\right| - \frac{\left|u_g\right|}{\left|Z_c\right|}. \tag{6}$$

In this paper, $|u_g| = 155$ V, $|i_{2ref}| = 20$ A. The error between $|i_{2ref}|$ and $|i_{1ref}|$ is only 0.23 A, which can be regarded as $i_{2ref} \approx i_{1ref}$. Therefore, Fig. 4 is approximated as Fig. 5.

In an ideal situation, the loop of the MPC controller can be regarded as a proportional component with $k = 1$. Hence, the path from i_1 to i_2 is equivalent to the closed-loop system of i_2, as shown in Fig. 6, where $G_z(s) = 1/sC$.

In the system without damping, the closed-loop transfer function $G_{i2cl}(s)$ is given by (7), and the Bode diagram of $G_{i2cl}(s)$ is shown in Fig. 7, where $L_2 + L_g = 0.6$ mH, $C = 4.7$ μF:

$$G_{i2cl}(s) = \frac{1}{s^2(L_2+L_g)C + 1}. \tag{7}$$

The resonance frequency f_r is given by

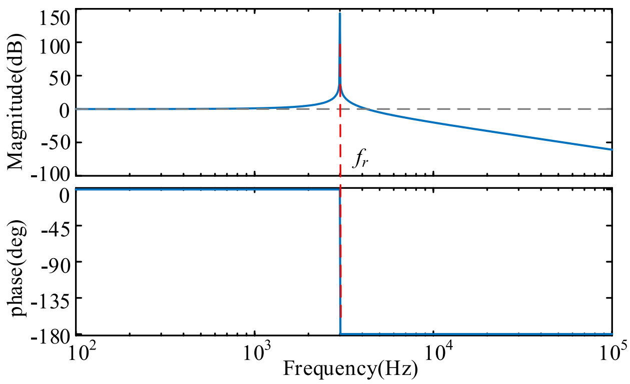

Fig. 7 Bode diagram of the closed-loop system without damping

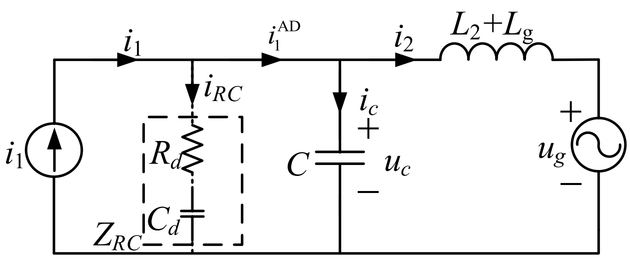

Fig. 8 Equivalent circuit of the system with virtual RC damping

$$f_r = \frac{1}{2\pi\sqrt{(L_2+L_g)C}}. \tag{8}$$

From (7), the closed-loop system has a pair of complex conjugate poles on the imaginary axis of the s-plane, which may impair the stability of the system. Moreover, the resonance peak at f_r can greatly amplify the inverter-side current harmonics to the grid side. Hence, additional AD is necessary.

3.2 Virtual RC damping for MPC Controller

To suppress the resonance peak and improve the performance of the system, a virtual RC damping is connected in parallel with the filter capacitor C as an AD. The improved circuit is shown in Fig. 8, and the new $G_z(s)$ is given by (9), where R_d is a virtual resistance, and C_d is a virtual capacitor:

$$G_z^{AD}(s) = \frac{sR_dC_d + 1}{s(sCR_dC_d + C + C_d)}. \tag{9}$$

The closed-loop transfer function of the system with virtual RC damping is given by

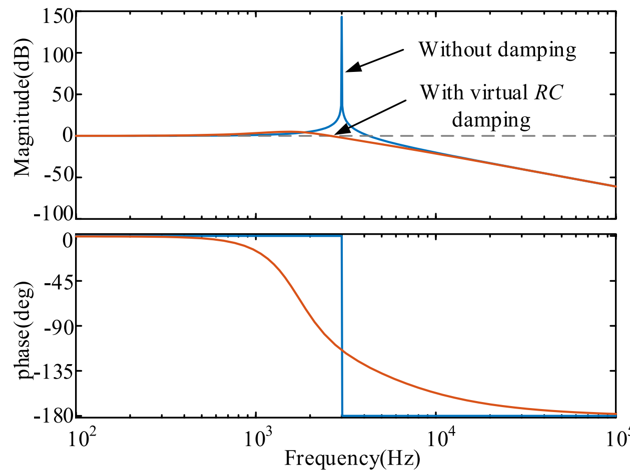

Fig. 9 Bode diagram of the closed-loop system with and without the virtual RC damping

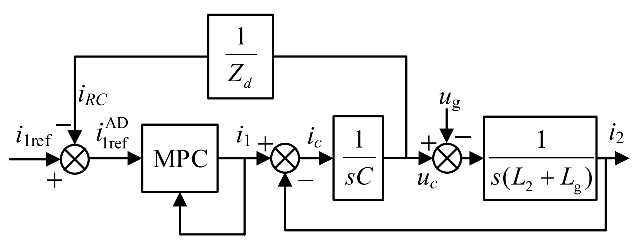

Fig. 10 Block diagram of the virtual RC damping for u_c feedback

$$G_{i2cl}^{AD}(s) = \frac{sR_dC_d + 1}{s^3(L_2+L_g)CR_dC_d + s^2(L_2+L_g)(C+C_d) + sR_dC_d + 1}. \tag{10}$$

The Bode diagram of $G_{i2cl}^{AD}(s)$ is shown in Fig. 9, where $R_d = 8\ \Omega$, $C_d = 20\ \mu F$. The resonance peak is effectively suppressed by the virtual RC damping, and the performance of the system is improved.

To add the virtual RC damping to the cost function, this paper uses the u_c feedback scheme to obtain the current reference i_{1ref}^{AD}. The principle of this method is shown in Fig. 10, where the virtual RC damping current i_{RC} is

$$i_{RC} = C_d\frac{d(u_c - i_{RC}R_d)}{dt}. \tag{11}$$

(11) is discretized by the backward difference scheme to obtain the $i_{RC}(k)$:

$$i_{RC}(k) = \frac{C_d\left(u_c(k) - u_c(k-1)\right) + R_dC_di_{RC}(k-1)}{T_s + R_dC_d}, \tag{12}$$

and the current reference with virtual RC damping at time k is given by

$$i_{1\mathrm{ref}}^{\mathrm{AD}}(k) = i_{1\mathrm{ref}}(k) - i_{\mathrm{RC}}(k). \quad (13)$$

With $i_{1\mathrm{ref}}(k)$ being replaced with $i_{1\mathrm{ref}}^{\mathrm{AD}}(k)$ in (4), the cost function with virtual RC damping is obtained:

$$g_j^{\mathrm{AD}} = \left(i_{1\mathrm{ref}}^{\mathrm{AD}}(k) - i_1(k+1)\right)^2. \quad (14)$$

4 Adaptive AD method for weak grid conditions

4.1 Influence of the varied grid impedance on the system

Under weak grid conditions, the performance of the system changes due to the variation of L_g. The Bode diagram and the performance parameters of the $G_{i2\mathrm{cl}}^{\mathrm{AD}}(s)$ for different L_g are shown in Fig. 11 and Table 1, respectively, where the values of R_d and C_d are both fixed ($R_d = 8\ \Omega$, $C_d = 20\ \mu\mathrm{F}$).

When $G_{i2\mathrm{cl}}^{\mathrm{AD}}(s)$ is regarded as the transfer function from i_1 to i_2, the magnitude of resonance peak M_r increases with the increase of L_g and reaches 10.5 dB when $L_g = 6$ mH. Under this condition, the current harmonics from i_1 are amplified 3.4 times at f_r. This finding shows that the resonance suppression of virtual RC damping is impaired due to the increase of L_g.

Moreover, when $G_{i2\mathrm{cl}}^{\mathrm{AD}}(s)$ is regarded as the closed-loop transfer function of i_2, the bandwidth f_{bw} decreases rapidly with the increase of L_g. Thus, the dynamic performance of the system worsens. To solve the problems above, this paper proposes an adaptive AD algorithm based on impedance identification. Therefore, the optimal virtual RC parameters can be calculated for different grid impedance values.

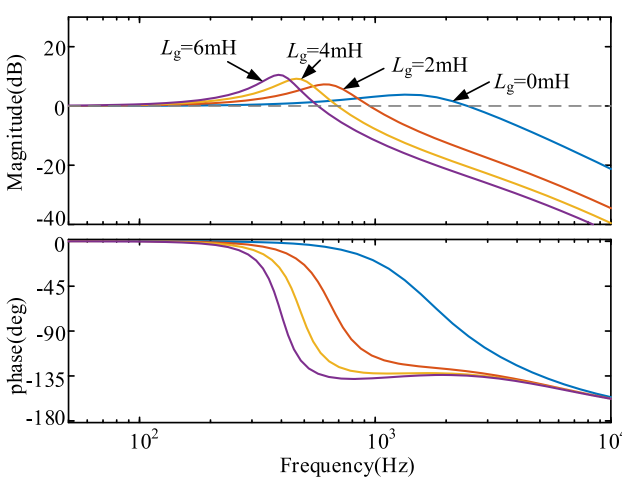

Fig. 11 Bode diagram of the closed-loop system with fixed-value AD for different L_g

Table 1 Performance parameters of the closed-loop system with fixed-value AD for different L_g

L_g/mH	f_{bw}/kHz	M_r/dB	f_r/kHz
0	3.11	3.83	1.33
2	1.09	7.28	0.62
4	0.78	9.20	0.46
6	0.64	10.50	0.39

4.2 Impedance identification of the weak grid

To obtain the grid impedance L_g, this paper uses non-characteristic harmonic injection [27] to measure the grid impedance online, as shown in Fig. 12, where $i_{\_75}$ is the current harmonic with a frequency of 75 Hz.

When $i_{\_75}$ is added to $i_{2\mathrm{ref}}$, the grid-side current i_2 contains the harmonic component at 75 Hz, and a response of u_{pcc} is generated at the same time. The amplitude and the phase of i_2 and u_{pcc} at 75 Hz are extracted by discrete Fourier transform, and the grid impedance L_g can be obtained by (15):

$$L_g = \frac{\sin \angle\varphi}{2\pi f_i} \frac{\left|\boldsymbol{u}_{\mathbf{pcc\_75}}\right|}{\left|\boldsymbol{i}_{\mathbf{2\_75}}\right|}, \quad (15)$$

where $f_i = 75$ Hz, $\boldsymbol{u}_{\mathbf{pcc\_75}}$ and $\boldsymbol{i}_{\mathbf{2\_75}}$ are the harmonic components of u_{pcc} and i_2 at 75 Hz, and φ is the phase difference between $\boldsymbol{u}_{\mathbf{pcc\_75}}$ and $\boldsymbol{i}_{\mathbf{2\_75}}$.

4.3 Calculation of virtual RC parameters

From (10), the characteristic equation $D(s)$ of the closed-loop system is

$$D(s) = s^3(L_2 + L_g)CR_dC_d + s^2(L_2 + L_g)(C + C_d) + sR_dC_d + 1. \quad (16)$$

An ideal third-order system should have one real pole and two complex conjugate poles on the left half of the s-plane. Thus, the ideal characteristic equation $D_r(s)$ is constructed by

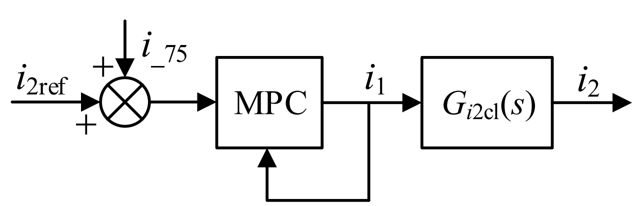

Fig. 12 Control block diagram of 75 Hz harmonic injection

$$D_r(s) = \left(s(L_2 + L_g)CR_dC_d + K\right)(s^2 + 2\zeta\omega_n s + \omega_n^2), \quad (17)$$

where ζ is the damping coefficient, and ω_n is the natural frequency. The 3 poles and 1 zero of the closed-loop system are calculated by

$$\begin{cases} z_1 = -\dfrac{1}{R_dC_d} \\ p_1 = -\dfrac{1}{(L_2 + L_g)CR_dC_d\omega_n^2}, \\ p_{2,3} = -\zeta\omega_n \pm \omega_n\sqrt{\zeta^2 - 1} \end{cases} \quad (18)$$

where z_1 is the real zero, p_1 is the real pole, and $p_{2,3}$ are the complex conjugate poles. With the ratio of the distance between p_1 and $p_{2,3}$ to the imaginary axis set as η, the ratio of the distance between p_1 and z_1 to the imaginary axis is λ:

$$\begin{cases} \eta = \dfrac{1}{(L_2 + L_g)CR_dC_d\zeta\omega_n^3}, \\ \lambda = 1 + 2\eta\zeta^2 \end{cases} \quad (19)$$

where ω_n is given by

$$\omega_n = \frac{1}{\sqrt{(1 + 2\eta\zeta^2)(L_2 + L_g)C}}. \quad (20)$$

With the combination of (16), (17), and (20), C_d and R_d are calculated by

$$\begin{cases} C_d = C\left(\dfrac{2\lambda}{\eta} + \lambda - 1\right) \\ R_d = \dfrac{2\zeta}{\omega_n C_d\left(1 - (L_2 + L_g)C\omega_n^2\right)} \end{cases}, \quad (21)$$

Table 2 Performance parameters of the closed-loop system with adaptive AD algorithm for different L_g

L_g/mH	f_{bw}/kHz	M_r/dB	f_r/kHz
0	3.31	3.04	1.36
2	1.59	3.04	0.66
4	1.19	3.04	0.49
6	1.00	3.04	0.41

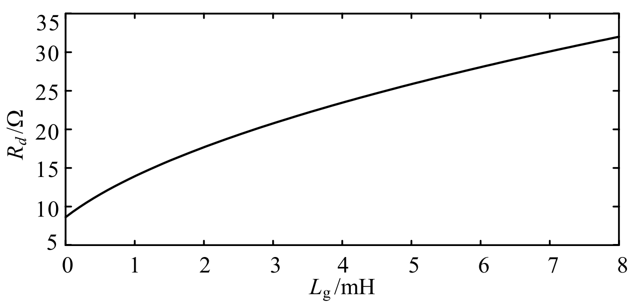

Fig. 13 Relationship between grid impedance L_g and virtual resistance R_d

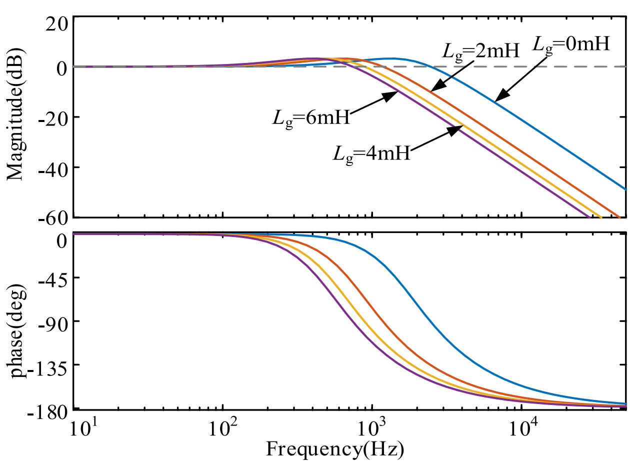

Fig. 14 Bode diagram of the closed-loop system with adaptive AD algorithm for different L_g

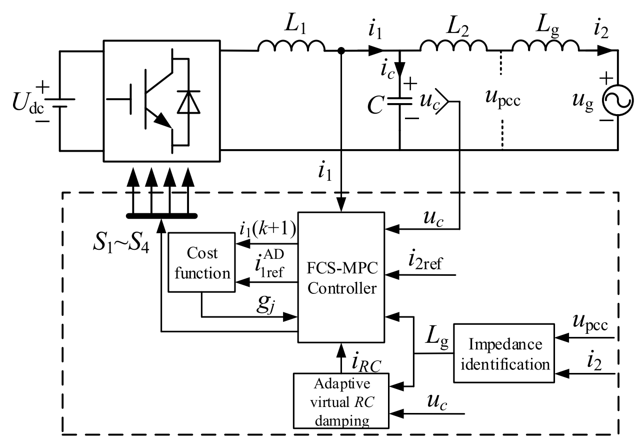

Fig. 15 Control block diagram of the single-phase LCL-type grid-connected inverter with adaptive AD strategy

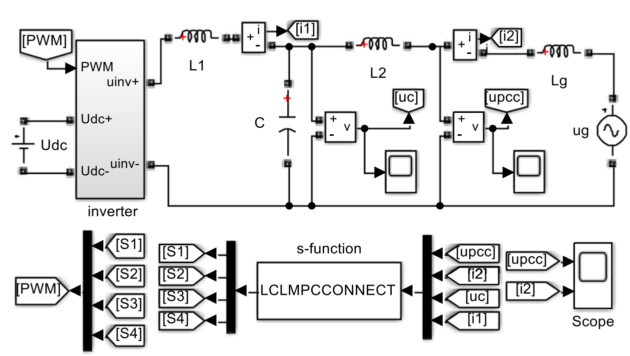

Fig. 16 Implementation of the system in MATLAB/Simulink

Fig. 17 Simulation waveforms and the spectrum of the grid-side current i_2 for different L_g: **a** $L_g = 0$ mH; **b** $L_g = 2$ mH; **c** $L_g = 4$ mH

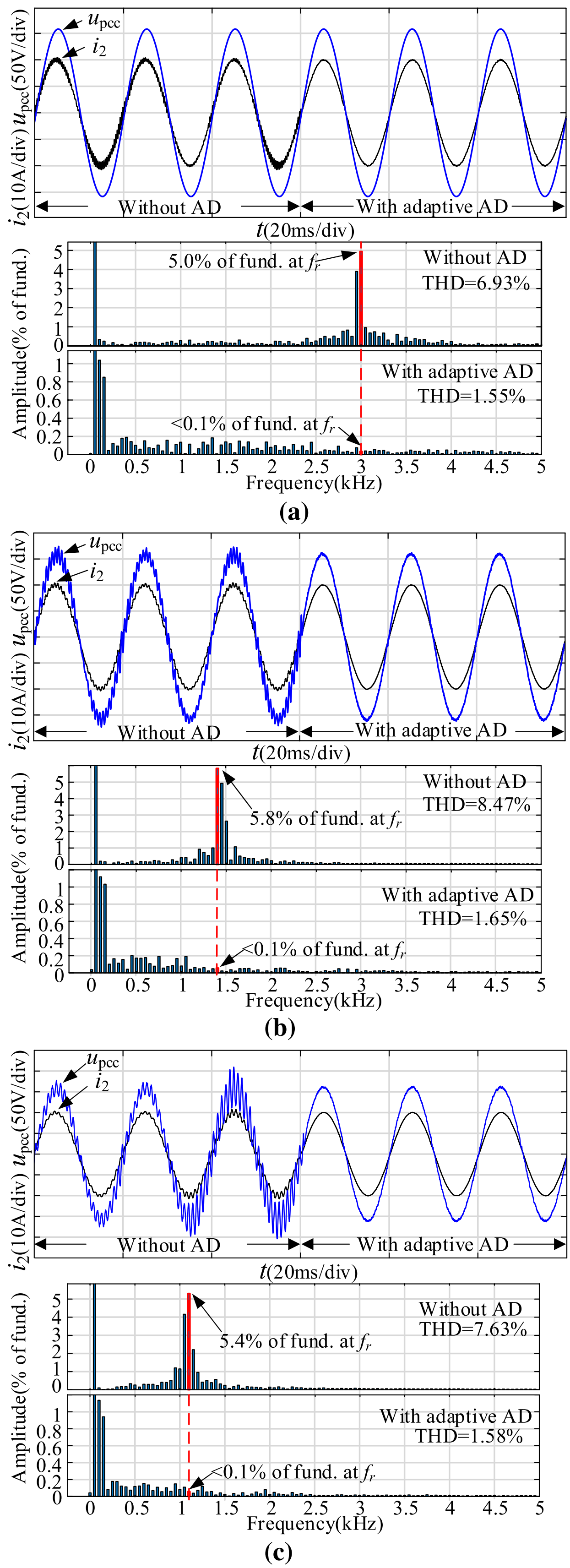

where η and λ determine the distribution of closed-loop poles on the s-plane and the performance of the system. $\eta = 1$ is set to ensure the damping and the response speed of the system. According to (19), the value of λ is always greater than 1. When λ approaches 1, p_1 and z_1 form a dipole, and the complex conjugate poles $p_{2,3}$ become the dominant poles. Thus, the damping ratio ζ and the resonance suppression are greatly reduced. When $\lambda \geq 3$, the complex conjugate pole disappears and the closed-loop poles consist of real poles only. Thus, the dynamic performance of the system is impaired. Consequently, setting $\lambda = 2$ balances the resonance suppression and dynamic performance.

From (21), if $\eta = 1$, $\lambda = 2$, $C = 4.7$ μF, then $C_d = 23.5$ μF. When C_d is obtained, the value of R_d is related to L_2 and L_g only. The relationship between L_g and R_d in the case of $L_2 = 0.6$ mH is shown in Fig. 13. The Bode diagram and the performance parameters of the closed-loop system with adaptive AD algorithm for different L_g are shown in Fig. 14 and Table 2, respectively.

As can be seen in Table 2, after the adaptive AD algorithm is added, the magnitude of the resonance peak M_r is maintained at 3.04 dB when L_g varies. For the case of $L_g = 6$ mH, compared with the system without adaptive AD algorithm (Fig. 11; Table 1), the M_r of the system with adaptive AD algorithm drops by 71.0%, and the closed-loop bandwidth f_{bw} increases by 56.3%. This result shows that the system with adaptive AD algorithm can balance the resonance suppression ability and dynamic performance under weak grid conditions. The overall control block diagram of the system is depicted in Fig. 15.

Table 3 Simulation parameters

Parameter	Value
DC-link voltage U_{dc}	200 V
Grid voltage (RMS) u_g	110 V
Inverter-side inductance L_1	3.6 mH
Grid-side inductance L_2	0.6 mH
Filter capacitor C	4.7 μF
Maximum switching frequency f_{smax}	20 kHz
Grid impedance L_g	0–4 mH

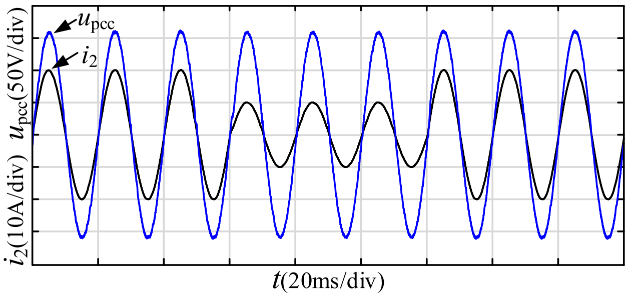

Fig. 18 Dynamic simulation results for $L_g = 4$ mH

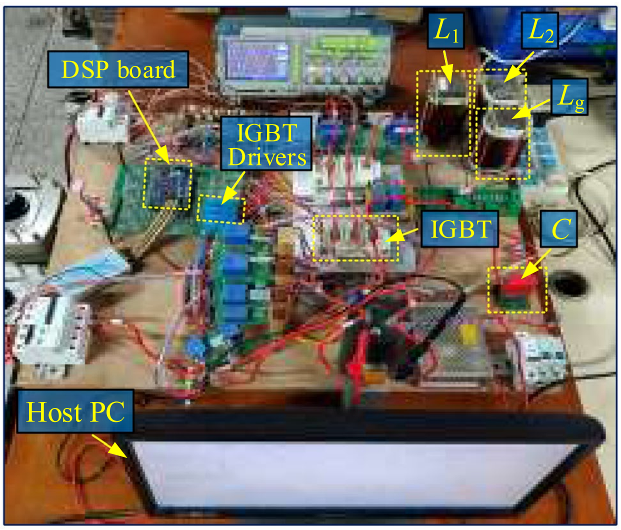

Fig. 19 Photograph of the experimental platform

5 Simulation and experimental results

5.1 Simulation results

The LCL-type grid-connected inverter model was built in MATLAB/Simulink according to Fig. 15, as shown in Fig. 16. The MPC controller and the adaptive AD are implemented in s-function, and the simulation parameters are shown in Table 3.

For the case of $L_g = 0$ mH, the simulation waveforms and the grid-side current spectrum are shown in Fig. 17a. When the system without AD, the harmonic amplitude of i_2 at f_r is 5.0% of the fundamental current (50 Hz), and the total harmonic distortion (THD) of i_2 is 6.93%. In contrast, for the system with the adaptive AD, the harmonic amplitude of i_2 at f_r is less than 0.1% of the fundamental current, and the THD of i_2 is reduced to 1.55%.

Figure 17b and c shows the simulation results for $L_g = 2$ mH and $L_g = 4$ mH, respectively. In the system without adaptive AD, the distortion of u_{pcc} becomes significant under weak grid conditions. The harmonic amplitude of i_2 at f_r is more than 5% of the fundamental current, and the THDs of i_2 are 8.47% ($L_g = 2$ mH) and 7.63% ($L_g = 4$ mH). After the adaptive AD is added, the distortion of u_{pcc} is greatly reduced and the THDs of i_2 drop to 1.65% ($L_g = 2$ mH) and 1.58% ($L_g = 2$ mH), respectively.

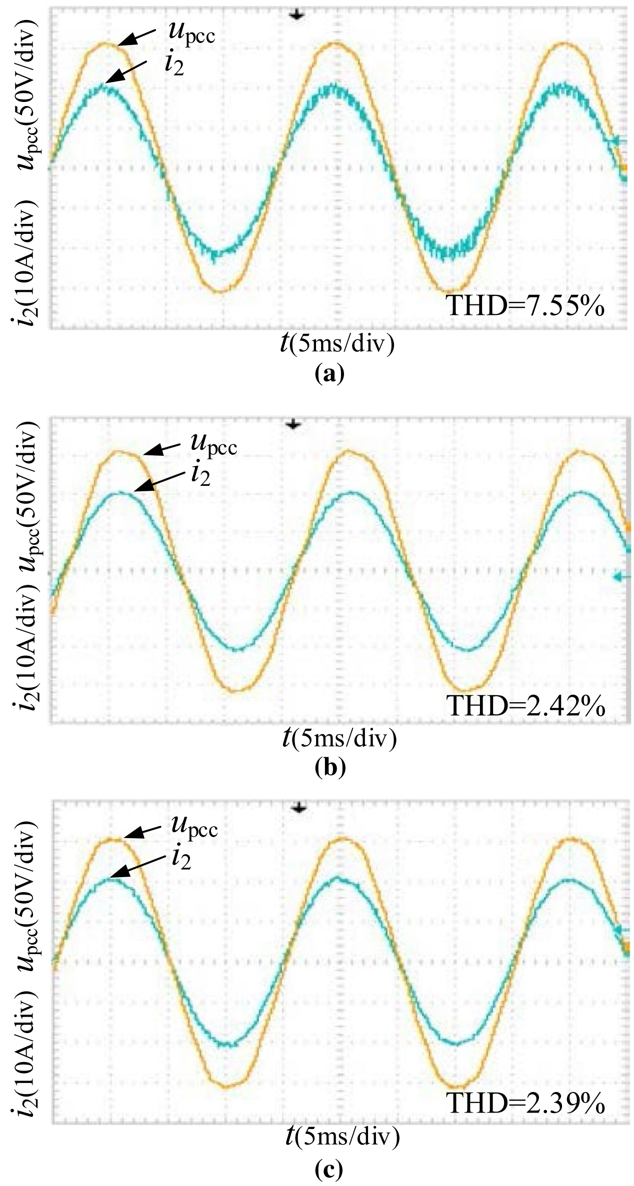

Fig. 20 Steady experimental results for $L_g = 0$ mH: **a** the system without AD; **b** the system with conventional VR AD; **c** the system with adaptive AD

To verify the dynamic performance of the system, a reference-value step of grid current ($|i_{2ref}|$ from 20 to 10 A) is applied for $L_g = 4$ mH, as shown in Fig. 18. The current step process is stable and has no oscillation, and the system has a good dynamic response.

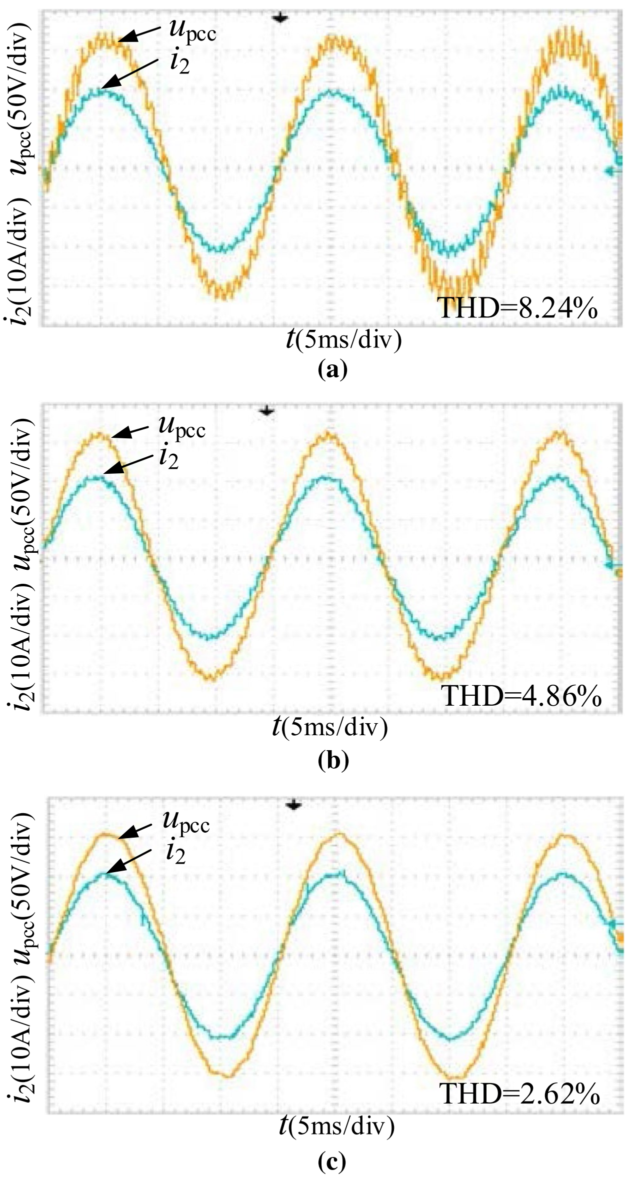

Fig. 21 Steady experimental results for $L_g = 2$ mH: **a** the system without AD; **b** the system with conventional VR AD; **c** the system with adaptive AD

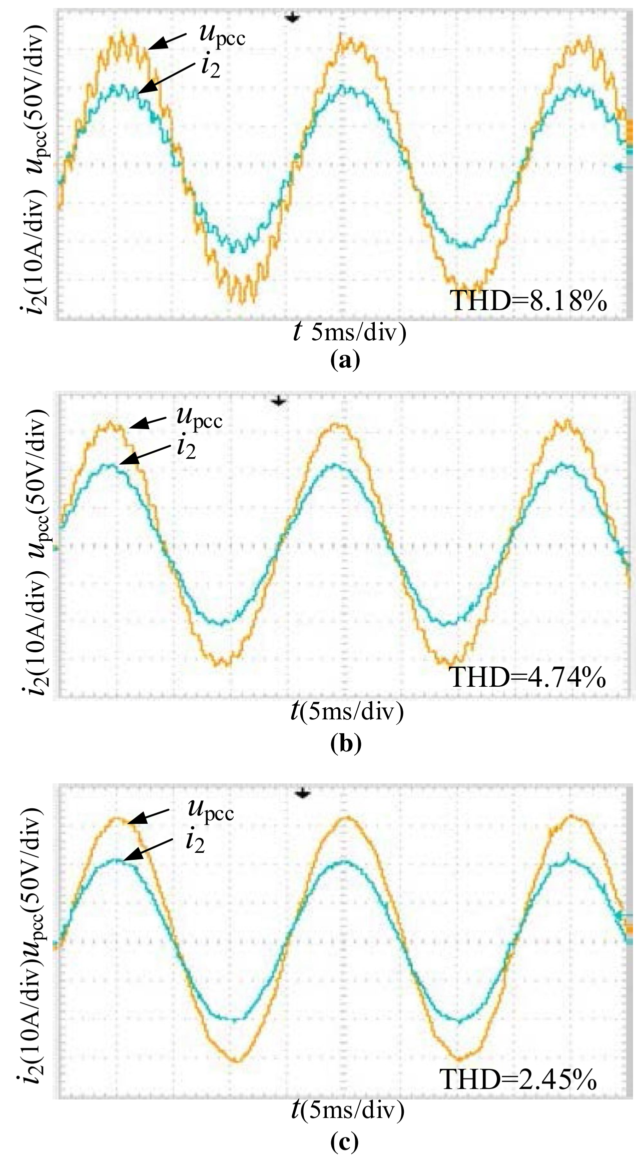

Fig. 22 Steady experimental results for $L_g = 4$ mH: **a** the system without AD; **b** the system with conventional VR AD; **c** the system with adaptive AD

5.2 Experimental results

To validate the practicability of the proposed method, a 2 kW LCL-type grid-connected inverter prototype was constructed, as shown in Fig. 19. The current controller is implemented on a DSP with TMS320F28335 for IGBT (Infineon FF100R12KS4) pulse signal generation, and the weak grid is composed of a voltage source (with a value of u_g) in series with an inductor (with a value of L_g). The experimental parameters are the same as the simulation parameters, as given in Table 3.

First, the system without AD, the system with conventional VR AD (the virtual resistance with a value of 30 Ω), and the system with proposed adaptive AD are compared under different grid conditions. In the steady-state experiment, the amplitude of the grid current reference value is 20 A. Figure 20 shows the experimental waveforms of the three methods under a strong grid condition ($L_g = 0$ mH). In the system without AD, the distortion of i_2 is obvious and the

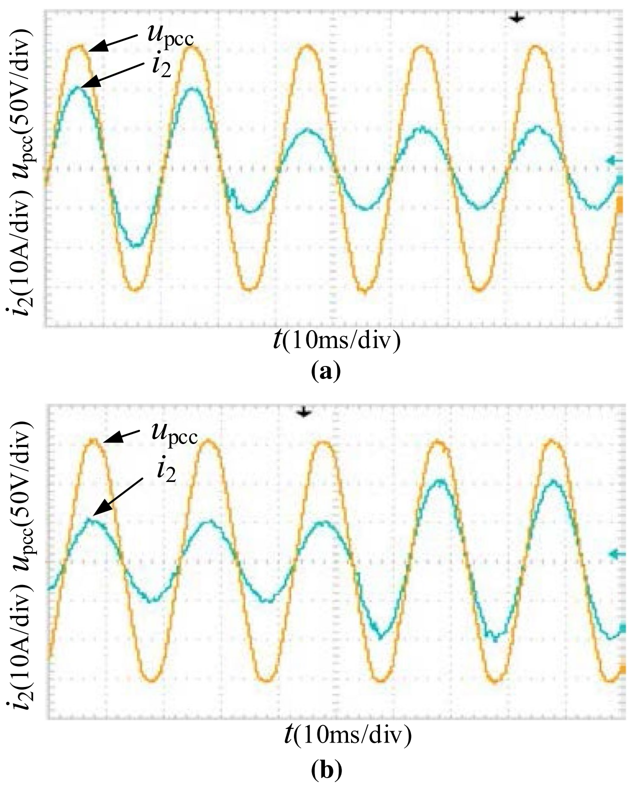

Fig. 23 Dynamic experimental results for $L_g = 4$ mH: **a** $|i_{2ref}|$ from 20 to 10 A; **b** $|i_{2ref}|$ from 10 to 20 A

THD of i_2 is 7.55%. In contrast, the grid current harmonics are effectively suppressed by adding the VR AD or the adaptive AD. The THDs of i_2 are reduced to 2.42% and 2.39%, respectively.

Figures 21a and 22a show the experimental waveforms of the system without AD under weak grid conditions. The u_{pcc} and i_2 are significantly distorted due to the grid impedance. The THDs of i_2 are 8.24% for $L_g = 2$ mH and 8.18% for $L_g = 4$ mH. Figures 21b and 22b show the experimental results of the system with conventional VR AD. Compared with the strong grid condition, the harmonic suppression capability of VR AD decreases because of the influence of grid impedance (the THDs of i_2 rise to 4.86% for $L_g = 2$ mH and to 4.74% for $L_g = 4$ mH). Figures 21c and 22c show the experimental results of the system with proposed adaptive AD. Compared with the two methods above, the adaptive AD improves the quality of the grid currents and reduces the THDs of i_2 to 2.62% ($L_g = 2$ mH) and 2.45% ($L_g = 4$ mH), respectively. The experimental results validate that when the grid impedance varies, adaptive AD can still suppress the grid current harmonics effectively.

To evaluate the dynamic performance of the system, a step in grid current reference i_{2ref} is shown in Fig. 23 for $L_g = 4$ mH. The peak of i_{2ref} changes from 20 to 10 A and 10–20 A, as shown in Fig. 23a and b respectively. The grid current can reach the given value rapidly with a small overshoot, and the system shows a fast dynamic response. Finally, on the basis of the experimental results, the advantages and disadvantages of the proposed method and the conventional methods are compared, as shown in Table 4.

6 Conclusion

This paper proposed an adaptive AD strategy for the grid-connected inverter based on FCS-MPC. The virtual RC damping method can effectively suppress the resonance peak of the LCL filter and reduce the impact of the variable switching frequency in the FCS-MPC-based system. Under weak grid conditions, the adaptive AD algorithm can obtain the optimal virtual RC value online. Unlike the fixed-value AD, the proposed method can maintain the resonance suppression of the virtual RC damping under different grid impedance values, and the system has higher bandwidth at the same time. The simulations and experimental results show that when the grid impedance varies, the proposed method can ensure the reduction of

Table 4 Comparison of the advantages and disadvantages of different control methods

Control methods	Advantages	Disadvantages
MPC controller without AD	1. Without additional damping; easy to implement	1. With low-quality grid currents
MPC controller with conventional VR AD	1. With fixed-value AD; the design of AD is simple 2. Provides high-quality grid currents under a strong grid condition ($L_g = 0$ mH)	1. The optimal AD parameters need to be obtained by trial-and-error 2. With low-quality grid currents under weak grid conditions ($L_g \geq 2$ mH)
MPC controller with proposed adaptive AD	1. With adaptive AD; the optimal AD parameters can be obtained by the adaptive algorithm 2. Provides high-quality grid currents under both strong and weak grid conditions	1. The analysis and design of the adaptive algorithm are more complex

grid current harmonics, and the system has good dynamic performance.

Acknowledgements This work was supported by the National Natural Science Foundation of China (51567004) and the High-level Innovation Team and Distinguished Scholar Program of Guangxi Higher Education Institutions under Grant Guangxi teach talent (2020) No. 6.

Declarations

Conflict of interest On behalf of all the authors, the corresponding author states that they have no conflict of interest.

References

1. Liserre, M., Teodorescu, R., Blaabjerg, F.: Stability of photovoltaic and wind turbine grid-connected inverters for a large set of grid impedance values. IEEE Trans. Power Electron. **21**(1), 263–272 (2006)
2. Vieira, R.P., Martins, L.T., Massing, J.R., Stefanello, M.: Sliding mode controller in a multiloop framework for a grid-connected VSI with LCL filter. IEEE Trans. Ind. Electron. **65**(6), 4714–4723 (2018)
3. Fu, X., Li, S.: Control of single-phase grid-connected converters with LCL filters using recurrent neural network and conventional control methods. IEEE Trans. Power Electron. **31**(7), 5354–5364 (2016)
4. Xia, C., Liu, T., Shi, T., Song, Z.: A simplified finite-control-set model-predictive control for power converters. IEEE Trans. Ind. Inform. **10**(2), 991–1002 (2014)
5. Aguilera, R.P., Quevedo, D.E.: Predictive control of power converters: designs with guaranteed performance. IEEE Trans. Ind. Inform. **11**(1), 53–63 (2015)
6. Ramírez, R.O., Espinoza, J.R., Baier, C.R., Rivera, M., Villarroel, F., Guzman, J.I., Melín, P.E.: Finite-state model predictive control with integral action applied to a single-phase z-source inverter. IEEE J. Emerg. Sel Top Power Electron. **7**(1), 228–239 (2019)
7. Vazquez, S., Zafra, E., Aguilera, R.P., Geyer, T., Leon, J.I., Franquelo, L.G.: Prediction model with harmonic load current components for FCS-MPC of an uninterruptible power supply. IEEE Trans. Power Electron. **37**(1), 322–331 (2022)
8. Hu, J., Zhu, J., Dorrell, D.G.: Model predictive control of grid-connected inverters for PV systems with flexible power regulation and switching frequency reduction. IEEE Trans. Ind. Appl. **51**(1), 587–594 (2015)
9. Baier, C.R., Ramirez, R.O., Marciel, E.I., Hernández, J.C., Melín, P.E., Espinosa, E.E.: FCS-MPC without steady-state error applied to a grid-connected cascaded H-bridge multilevel inverter. IEEE Trans. Power Electron. **36**(10), 11785–11799 (2021)
10. Aguirre, M., Kouro, S., Rojas, C.A., Vazquez, S.: Enhanced switching frequency control in FCS-MPC for power converters. IEEE Trans. Ind. Electron. **68**(3), 2470–2479 (2021)
11. Young, H.A., Perez, M.A., Rodriguez, J.: Analysis of finite-control-set model predictive current control with model parameter mismatch in a three-phase inverter. IEEE Trans. Ind. Electron. **63**(5), 3100–3107 (2016)
12. Lim, C.S., Goh, H.H., Lee, S.S.: Long-prediction-horizon near-optimal model predictive grid current control for PWM-Driven VSIs with LCL filters. IEEE Trans. Power Electron. **36**(2), 2246–2257 (2021)
13. Chen, X., Wu, W., Gao, N., Chung, H.S.H., Liserre, M., Blaabjerg, F.: Finite control set model predictive control for LCL-filtered grid-tied inverter with minimum sensors. IEEE Trans. Ind. Electron. **67**(12), 9980–9990 (2020)
14. Panten, N., Hoffmann, N., Fuchs, F.W.: Finite control set model predictive current control for grid-connected voltage-source converters with LCL filters: a study based on different state feedbacks. IEEE Trans. Power Electron. **31**(7), 5189–5200 (2016)
15. Xue, C., Zhou, D., Li, Y.: Hybrid model predictive current and voltage control for LCL-filtered grid-connected inverter. IEEE J. Emerg. Sel. Top. Power Electron. **9**(5), 5747–5760 (2021)
16. Peña-Alzola, R., Liserre, M., Blaabjerg, F., Ordonez, M., Yang, Y.: LCL-filter design for robust active damping in grid-connected converters. IEEE Trans. Ind. Inform. **10**(4), 2192–2203 (2014)
17. Bao, C., Ruan, X., Wang, X., Li, W., Pan, D., Weng, K.: Step-by-step controller design for LCL-type grid-connected inverter with capacitor–current-feedback active-damping. IEEE Trans. Power Electron. **29**(3), 1239–1253 (2014)
18. Pan, D., Ruan, X., Bao, C., Li, W., Wang, X.: Optimized controller design for LCL-type grid-connected inverter to achieve high robustness against grid-impedance variation. IEEE Trans. Ind. Electron. **62**(3), 1537–1547 (2015)
19. Xin, Z., Loh, P.C., Wang, X., Blaabjerg, F., Tang, Y.: Highly accurate derivatives for LCL-filtered grid converter with capacitor voltage active damping. IEEE Trans. Power Electron. **31**(5), 3612–3625 (2016)
20. Rodriguez-Diaz, E., Freijedo, F.D., Vasquez, J.C., Guerrero, J.M.: Analysis and comparison of notch filter and capacitor voltage feedforward active damping techniques for LCL grid-connected converters. IEEE Trans. Power Electron. **34**(4), 3958–3972 (2019)
21. Massing, J.R., Stefanello, M., Grundling, H.A., Pinheiro, H.: Adaptive current control for grid-connected converters with LCL filter. IEEE Trans. Ind. Electron. **59**(12), 4681–4693 (2012)
22. Cortes, P., Rodriguez, J., Quevedo, D.E., Silva, C.: Predictive current control strategy with imposed load current spectrum. IEEE Trans. Power Electron. **23**(2), 612–618 (2008)
23. Ferreira, S.C., Gonzatti, R.B., Pereira, R.R., Silva, C.H.D., Silva, L.E.B., Lambert-Torres, G.: Finite control set model predictive control for dynamic reactive power compensation with hybrid active power filters. IEEE Trans. Ind. Electron. **65**(3), 2608–2617 (2018)
24. Scoltock, J., Geyer, T., Madawala, U.K.: A model predictive direct current control strategy with predictive references for MV grid-connected converters with LCL-filters. IEEE Trans. Power Electron. **30**(10), 5926–5937 (2015)
25. Zhang, X., Wang, Y., Yu, C., Guo, L., Cao, R.: Hysteresis model predictive control for high-power grid-connected inverters with output LCL filter. IEEE Trans. Ind. Electron. **63**(1), 246–256 (2016)
26. Serpa, L.A., Ponnaluri, S., Barbosa, P.M., Kolar, J.W.: A modified direct power control strategy allowing the connection of three-phase inverters to the grid through LCL filters. IEEE Trans. Ind. Appl. **43**(5), 1388–1400 (2007)
27. Asiminoaei, L., Teodorescu, R., Blaabjerg, F., Borup, U.: Implementation and test of an online embedded grid impedance estimation technique for PV inverters. IEEE Trans. Ind. Electron. **52**(4), 1136–1144 (2005)

Ruinan Xue received his B.S. degree in electrical engineering and automation from Lanzhou University of Technology, Lanzhou, China, in 2018. He is currently pursuing his M.S. degree in Electrical Engineering at Guangxi University, Nanning, China. His research interests include power electronics, renewable energy, and power converters for microgrids.

Hengzhou Tong received his B.S. degree in Electrical Engineering and Automation from Chang'an University, Xi'an, China, in 2019. He is currently pursuing his M.S. degree in Electrical Engineering at Guangxi University, Nanning, China. His research interests include power electronics, electromagnetic interference, and DC–DC converters.

Guojin Li received his Ph.D. degree from South China University of Technology, Guangzhou, China, in 2006. He is currently a professor at the School of Electrical Engineering, Guangxi University. His research interests include high-efficiency DC–DC conversions for high-power and energy applications.

Yanming Chen received his Ph.D. degree from South China University of Technology, Guangzhou, China, in 1998. Since 2006, he has been a full professor with the School of Electrical Engineering, Guangxi University. His current research interests include soft-switching power converters and high-frequency DC–DC converters.